



**HAL**  
open science

## Innovative ochre processing and tool use in China 40,000 years ago

Fa-Gang Wang, Shi-Xia Yang, Jun-Yi Ge, Andreu Ollé, Ke-Liang Zhao, Jian-Ping Yue, Daniela Eugenia Rosso, Katerina Douka, Ying Guan, Wen-Yan Li, et al.

### ► To cite this version:

Fa-Gang Wang, Shi-Xia Yang, Jun-Yi Ge, Andreu Ollé, Ke-Liang Zhao, et al.. Innovative ochre processing and tool use in China 40,000 years ago. *Nature*, 2022, 603 (7900), pp.284-289. 10.1038/s41586-022-04445-2. hal-03860971

**HAL Id: hal-03860971**

**<https://hal.science/hal-03860971v1>**

Submitted on 23 Oct 2023

**HAL** is a multi-disciplinary open access archive for the deposit and dissemination of scientific research documents, whether they are published or not. The documents may come from teaching and research institutions in France or abroad, or from public or private research centers.

L'archive ouverte pluridisciplinaire **HAL**, est destinée au dépôt et à la diffusion de documents scientifiques de niveau recherche, publiés ou non, émanant des établissements d'enseignement et de recherche français ou étrangers, des laboratoires publics ou privés.



Distributed under a Creative Commons Attribution 4.0 International License

1 To cite this article, please quote:” Wang, FG., Yang, SX., Ge, JY. *et al.* Innovative ochre processing and  
2 tool use in China 40,000 years ago. *Nature* 603, 284–289 (2022). [https://doi.org/10.1038/s41586-022-](https://doi.org/10.1038/s41586-022-04445-2)  
3 [04445-2](https://doi.org/10.1038/s41586-022-04445-2)”

4

## 5 **Innovative ochre processing and tool use in China ~40,000 years ago**

6 Fa-Gang Wang<sup>1†</sup>, Shi-Xia Yang<sup>2,3,4,5†\*</sup>, Jun-Yi Ge<sup>2,3</sup>, Andreu Ollé<sup>6,7</sup>, Ke-Liang Zhao<sup>2,3</sup>, Jian-  
7 Ping Yue<sup>8</sup>, Daniela Eugenia Rosso<sup>9,10</sup>, Katerina Douka<sup>4,11</sup>, Ying Guan<sup>2,3</sup>, Wen-Yan Li<sup>1</sup>, Hai-  
8 Yong Yang<sup>12</sup>, Lian-Qiang Liu<sup>1</sup>, Fei Xie<sup>1</sup>, Zheng-Tang Guo<sup>13</sup>, Ri-Xiang Zhu<sup>14</sup>, Cheng-Long  
9 Deng<sup>14,15\*</sup>, Francesco d’Errico<sup>16,17\*</sup>, Michael Petraglia<sup>4,18,19,20\*</sup>

10 <sup>1</sup>Hebei Provincial Institute of Cultural Relics and Archeology, Shijiazhuang 050031, China.

11 <sup>2</sup>Key Laboratory of Vertebrate Evolution and Human Origins, Institute of Vertebrate  
12 Palaeontology and Palaeoanthropology, Chinese Academy of Sciences, Beijing 100044, China.

13 <sup>3</sup>Center for Excellence in Life and Palaeoenvironment, Chinese Academy of Sciences, Beijing  
14 100044, China.

15 <sup>4</sup>Department of Archaeology, Max Planck Institute for the Science of Human History, Jena  
16 07745, Germany.

17 <sup>5</sup>State Key Laboratory of Loess and Quaternary Geology, Institute of Earth Environment,  
18 Chinese Academy of Sciences, Xi’an 710061, China.

19 <sup>6</sup>Institut Català de Palaeoecologia Humana i Evolució Social (IPHES-CERCA), Zona  
20 Educacional 4, Campus Sescelades URV (Edifici W3), 43007, Tarragona, Spain.

21 <sup>7</sup>Universitat Rovira i Virgili, Dept. d’Història i Història de l’Art, Av. Catalunya 35, 43002,  
22 Tarragona, Spain.

23 <sup>8</sup>Department of History, Anhui University, Hefei 230039, China.

24 <sup>9</sup>Université Côte d’Azur, CNRS, CEPAM, Nice, France.

25 <sup>10</sup>Departament de Prehistòria, Arqueologia i Història Antiga, Grupo de Investigación Prehistoria  
26 del Mediterráneo Occidental (PREMEDOC), Universitat de València, Valencia, Spain.

27 <sup>11</sup>Oxford Radiocarbon Accelerator Unit, Research Laboratory for Archaeology and the History  
28 of Art, University of Oxford, Oxford, OX1 3TG, UK.

29 <sup>12</sup>Museum of Yuzhou, Yuxian 075700, China.

30 <sup>13</sup>Key Laboratory of Cenozoic Geology and Environment, Institute of Geology and Geophysics,  
31 Chinese Academy of Sciences, Beijing 100029, China.

32 <sup>14</sup>State Key Laboratory of Lithospheric Evolution, Institute of Geology and Geophysics, Chinese  
33 Academy of Sciences, Beijing 100029, China.

34 <sup>15</sup>College of Earth and Planetary Sciences, University of Chinese Academy of Sciences, Beijing  
35 100049, China.

36 <sup>16</sup>PACEA UMR 5199, Université de Bordeaux, CNRS, Pessac, France.

37 <sup>17</sup>SFF Centre for Early Sapiens Behaviour (SapienCE), University of Bergen, Bergen, Norway.

38 <sup>18</sup>Human Origins Program, National Museum of Natural History, Smithsonian Institution,  
39 Washington, D.C. 20560, USA.

40 <sup>19</sup>School of Social Science, The University of Queensland, Brisbane, Queensland 4072, Australia.

41 <sup>20</sup>Australian Research Centre for Human Evolution (ARCHE), Griffith University, Brisbane,  
42 Australia.

43 †These authors contributed equally to this work.  
44 \* Corresponding authors. yangshixia@ivpp.ac.cn (S.X.Y.), cldeng@mail.iggcas.ac.cn (C.L.D.),  
45 francesco.derrico@u-bordeaux.fr (F.D.), petraglia@shh.mpg.de (M.P.).

46  
47  
48 *Homo sapiens* was present in northern Asia by ~40,000 years ago, having ultimately replaced  
49 archaic populations in Eurasia after episodes of earlier population expansions and  
50 interbreeding<sup>1-4</sup>. Cultural adaptations associated with the last Neanderthals, Denisovans and the  
51 incoming populations of *H. sapiens* into Asia remain elusive<sup>1,5-7</sup>. Here, we describe Xiamabei, a  
52 well-preserved, ~40,000-year-old archaeological site in northern China, containing the earliest  
53 known ochre processing feature in Eastern Asia together with a distinctive miniaturized lithic  
54 assemblage, with bladelet-like tools bearing traces of hafting, and a bone tool. The cultural  
55 assembly of traits at Xiamabei is unique for Eastern Asia and does not correspond with those  
56 found at other archaeological site assemblages inhabited by archaic populations or to those  
57 generally associated with the expansion of *H. sapiens*, such as the Initial Upper Palaeolithic<sup>8-10</sup>.  
58 The record of northern Asia supports a process of cultural diversification and innovations  
59 emerging in a period of hominin hybridization and admixture<sup>2,6,7,11</sup>.

60

61

## 62 **Main Text**

63 One of the most profound events in human evolution was the worldwide expansion of *Homo*  
64 *sapiens*<sup>1,5,12</sup>. Fossil, genetic and archaeological evidence indicates that *H. sapiens* dispersed out  
65 of Africa multiple times over the last ~200 thousand years (ka)<sup>1,13</sup>, interbreeding with archaic  
66 hominins, such as the Neanderthals and Denisovans as they migrated across Eurasia<sup>6,8,14</sup>. Current  
67 palaeoanthropological and archaeological evidence demonstrates that *H. sapiens* was present in  
68 northern Asia by at least 40 ka ago<sup>2-4</sup>. It is often argued that the terrestrial expansion of modern  
69 humans was facilitated by the use of advanced economic, social and symbolic adaptations  
70 allowing occupation of a variety of ecosystems<sup>14</sup>. Pigment use, in particular, is seen as a key  
71 indicator of symbolically mediated behaviour<sup>15-17</sup>, and technological innovations, such as the use  
72 of miniaturised technology, is considered to have had adaptive and economic advantages<sup>18,19</sup>.  
73 Archaeological data, however, remain ambiguous as to the arrival of *H. sapiens* populations in  
74 China (Supplementary Information A). With the exception of Initial Upper Palaeolithic (IUP)  
75 and Mousterian toolkits in the Altai and Siberia, and a few sites in northern China<sup>20-22</sup>, little is

76 known about stone tool industries in Eastern Asia until microblade assemblages become the  
77 dominant technology after 29 ka<sup>9,23,24</sup>. With respect to possible evidence for early symbolism,  
78 only two engraved bones are known, one bearing residues of ochre, from northern China (ca.  
79 125–105 ka), interpreted as the product of archaic hominins<sup>25</sup>. Most artefacts signaling symbolic  
80 practices are much younger, and likely linked to *H. sapiens*, such as pendants and ochre at  
81 Zhoukoudian Upper Cave (ca. 35.1–33.5 ka)<sup>4</sup> and beads at Shuidonggou 2 (SDG 2) (ca. 31 ka)<sup>23</sup>.  
82 Beads, pendants, and figurines become common after ca. 29 ka, when microblade technology  
83 began to spread across northern China<sup>26–28</sup>.

84 Here we report the results of archaeological findings at Xiamabei, a newly excavated and  
85 well-preserved site in the Nihewan Basin of northern China (Fig. 1). Xiamabei contains the  
86 earliest evidence of ochre processing, a novel miniaturized lithic technology, with bladelet-like  
87 forms and hafted items, and a bone tool, dating to ~41–39 ka. Xiamabei stands apart from any  
88 other known archaeological site in China as it possesses a novel set of cultural characteristics at  
89 an early date. Located at the transition zone between the Inner Mongolian Plateau and North  
90 China Plain, the site offers important new insights in the expansion of *H. sapiens* along the  
91 northern route<sup>10</sup>.

92 Xiamabei is on the southern bank of the Huli River, where excavations were initiated in  
93 2013 in the form of a trench exposing a 12 m<sup>2</sup> area (Supplementary Information B). The  
94 stratigraphy, extending to a depth of 290 cm, encompasses six main layers in a floodplain  
95 environment (Fig. 2). Layer 6, the main cultural horizon, 10–20 cm in thickness, is composed of  
96 dark brown silty sediment, with occasional clay and sand aggregates. Layer 6 revealed evidence  
97 for ochre use and processing, a charcoal-rich hearth, 382 miniaturized lithics, a single bone tool  
98 (Extended Data Fig. 1) and 437 mammal bones (Fig. 1b–d). Characterization methods were  
99 applied to sediment samples, ochre items, the bone tool, and a sample of the miniaturized lithics.  
100 Accelerator mass spectrometry (AMS) <sup>14</sup>C and optically stimulated luminescence (OSL) dating  
101 yielded ages ranging between ca. 43 ka to 28 ka for the sequence, with the Layer 6 cultural  
102 horizon dating to ca. 41–39 ka (Fig. 2, Supplementary Information C).

103 Pollen from Layer 6 indicates a steppe landscape with patches of coniferous forest  
104 dominated by *Pinus*. The pollen assemblages and high *Artemisia*/Chenopodiaceae (A/C) ratio in  
105 Layer 6 indicate a relatively cool and semi-arid climate during the site occupation  
106 (Supplementary Information D). Faunal remains were highly fragmentary, with only 7.19%

107 being taxonomically identifiable. The presence of horse, deer and zokor is consistent with the  
108 pollen evidence, reflecting a steppe landscape with patches of forest (Supplementary Information  
109 D). The bulk of the mammalian fossils were less than 20 mm in length and most were burnt,  
110 some even highly carbonized, suggesting their possible use as fuel (Supplementary Information  
111 D2). Cutmarks were identified on two faunal fragments indicating that lithics were used to  
112 process carcasses. A single bone tool bearing traces of use wear in the form of microflake scars  
113 and polishing at one end, and regularization by scraping at the other end, possibly to facilitate  
114 prehension or hafting, was recovered from Layer 6. The tool represents one of the earliest  
115 examples in northern China for the working of bone with techniques proper to this raw material  
116 (Extended Data Fig. 1).

117

### 118 **Ochre processing evidence**

119 Evidence for ochre processing at Xiamabei consists of three artefacts lying in close spatial  
120 association and on a spot of red stained sediment whose colouration reduces in intensity on the  
121 objects (Fig. 3, Extended Data Figs. 2–5, Supplementary Information E and F). The three  
122 artefacts (Figs. 3a, b) consist of an ochre piece (OP1) consisting of an allochthonous hard iron-  
123 rich nodule bearing clear traces of having been repeatedly abraded to produce a bright dark red  
124 ochre powder (Fig. 3c), a smaller and more friable ochre piece (OP2) of a different composition  
125 (Fig. 3d), resulting from crushing an original larger piece to produce ochre powder, and an  
126 elongated limestone slab (LS) with smoothed areas stained with ochre (Fig. 3e) and preserving  
127 residues of hematite-rich ochre (Fig. 3f) similar to that composing the smaller ochre piece. No  
128 ochre residues were identified on an associated quartzite cobble (QC) bearing evidence of use as  
129 a pestle (Fig. 3g).

130 X-ray diffraction (XRD), Micro Raman spectroscopy (MR), Micro-X-ray fluorescence  
131 (Micro-XRF), mineral magnetism (MM), scanning electron microscopy coupled with energy  
132 dispersive spectroscopy (SEM-EDS) were applied to 12 sediment samples from inside and  
133 outside the red stained area on which the ochre pieces and associated artefacts were lying  
134 (Extended Data Fig. 6, Supplementary Information G). In contrast to samples located at various  
135 distances from the red stained area, two samples from inside the area are rich in FeO and contain  
136 abundant microfragments of hematite-rich rocks. This indicates that the reddish colour of the

137 sediment (on which the stone artefacts and the ochre fragments were laying) is due to the  
138 presence of diffuse ochre particles.

139 Taken together, the evidence indicates that different types of ochre were brought to the site  
140 and processed using abrasion and pounding to produce ochre powder of different colour and  
141 granulometry. Although the purpose of such an activity cannot be established (e.g., the  
142 production of paint for colouring objects or decorating bodies, tanning of hides, using ochre as a  
143 loading agent for adhesives), the quantity of ochre powder produced was large enough for the  
144 leftover to permanently impregnate the sediment of the area on which tasks took place. This  
145 work area, which represents the earliest known instance of ochre processing in Eastern Asia<sup>28</sup>,  
146 indicates that the use of this material was part of the behavioural repertoire of regional  
147 populations by ~40 ka, preceding the origin of microblade technologies in China by 10,000 years.

148

#### 149 **Novel miniaturized lithic assemblage with hafting evidence**

150 The Xiamabei lithic assemblage, composed of 382 artefacts, is a novel technology for northern  
151 China, especially in consideration of its age. Most of the lithic artefacts (94%) are smaller than  
152 40 mm and 58.37% (n=209) are smaller than 20 mm. Locally available small chert nodules and  
153 quartz pebbles dominate the lithic assemblage, though porphyry pebbles were also sometimes  
154 used. Freehand Hard Hammer Percussion (FHHP) and Bipolar Percussion (BP) methods were  
155 the main reduction techniques, as shown by the coexistence of flake-cores with pronounced  
156 Hertzian initiations and bipolar pieces with evidence of crushing on opposed platforms and  
157 diffuse bulbs of percussion (Supplementary Information H). BP is the predominant reduction  
158 technique, contributing to 70.11% of the identifiable specimens. The maximum length and width  
159 of BP cores were not significantly smaller than the FHHP cores, indicating that although hand-  
160 held flaking of small cores was possible, preference was given to bipolar reduction. Bipolar  
161 splinters had an average width of 13.59 mm (29.5% smaller than 10 mm), falling within the  
162 width range of formal microblades from younger sites in northern China<sup>29</sup>. BP reduction  
163 strategies therefore resulted in the efficient production of bladelet-like blanks that could be used  
164 as tools, with lengths frequently measuring 20 mm or less (Fig. 4)<sup>30</sup>.

165 In contrast to both earlier and contemporary lithic assemblages from the Nihewan  
166 Basin<sup>31,32</sup> retouched tools are exceedingly rare at Xiamabei. Only three pieces in the Xiamabei  
167 assemblage show formal edge modification: two denticulates and one slightly retouched end-

168 scraper. Functional analysis conducted on a selected sample of lithics, including 13 bipolar and 4  
169 FHHP products, identified use-wear on most of them (Supplementary Information D). Seven  
170 pieces show clear evidence of hafting based on the arrangement of micro-scarring, the absence of  
171 use-wear on areas covered by the hafting material, and the frequent presence of plant fiber  
172 imprints, pointing to the use of binding elements (Fig. 4). Bone hafts have been identified in two  
173 cases and exceptionally illustrated by a bladelet-like piece recovered with a portion of the haft  
174 still in place (Fig. 4a, Extended Data Figs. 7–9). Wear patterns indicate the hafted pieces were  
175 used for a variety of purposes including hide scraping, boring and scraping against hard matter  
176 (likely wood), whittling soft plant material, and probably cutting soft animal matter. Two pieces  
177 bearing an end-scraper outline were used in a manner consistent with classic Upper Palaeolithic  
178 hide working tools, although only one of the implements showed formal distal retouch (Fig. 4b).  
179 Use-wear on unhafted pieces complete the range of identified activities - mainly represented by  
180 cutting actions on different materials, boring on a hard material, and in two cases, as wedges on  
181 quartz flakes. Overall, the microscopic analyses indicated that the Xiamabei artefacts, including  
182 bladelet-like tools manufactured by the BP technique, were used in a variety of activities  
183 (Extended Data Fig. 10). In addition, ten artefacts with ochre residues, mainly in the form of  
184 dispersed particles, were identified. On four pieces, residues were associated with the hafted area,  
185 and on two pieces hide working was identified as residues were located on the active edge.  
186 Ochre may have been used as an additive for hide working or as a loading agent for a hafting  
187 adhesive.

188

### 189 **Implications for cultural adaptations in Eastern Asia**

190 The Xiamabei site excavations and analyses identifies the appearance, ~40,000 years ago, of new  
191 cultural features that were either unknown or exceedingly rare in this region and in the  
192 neighboring regions. The combination of two knapping techniques for the production of small  
193 blanks, used for a variety of tasks and sometimes hafted, indicates the existence of a complex  
194 technical system involving the use and transformation of different raw materials. Such a  
195 technical system, not identified at older and penecontemporaneous sites, gives the Xiamabei  
196 assemblage an original character. A workshop for the production and use of mineral pigments at  
197 Xiamabei constitutes a second new cultural element in comparison with earlier and  
198 contemporary sites. The use of ochre is not, however, associated with ostrich egg beads and

199 pierced teeth and shells found in younger sites, nor with the arrival, attested at younger sites, of  
200 microblade technology. Although the taxonomic affiliation of the human group that occupied  
201 Xiamabei ~40,000 years ago is not known, and an occupation by late Denisovans or even  
202 Neanderthals cannot be excluded, the most parsimonious hypothesis, considering the presence of  
203 contemporary fossils of modern humans at Tianyuandong<sup>2</sup>, and somewhat younger at Salkhit<sup>3</sup>  
204 and Zhoukoudian Upper Cave<sup>4</sup>, is that the visitors to Xiamabei were *H. sapiens*.

205         The way in which key cultural innovations emerged in different regions of the world  
206 remains unclear. For some regions, such as Africa, a discontinuous and regionally variable  
207 accretion model has been proposed, indirectly linked to the long and complex process that has  
208 led to the emergence of our species in that continent<sup>33</sup>. It has been argued that packages of  
209 innovations originally developed in Africa or elsewhere may have been introduced by the spread  
210 of modern humans into Eurasia. This is the model most often favoured for Asia, a region in  
211 which, following European trends, blade and microblade technology, personal ornaments, ochre  
212 use and complex bone technologies are seen as the signature of incoming *H. sapiens* populations.

213         The record emerging from northern China challenges dominant paradigms by showing  
214 that during a critical time window, at ca. 40 ka, a variety of cultural adaptations existed. The  
215 occurrence of a varied, though more simple lithic technology when compared to bladelet  
216 production, associated with previously unrecorded hafting techniques, and the presence of some  
217 innovations (ochre use, an expedient bone tool), and not others (formal bone tools, ornaments),  
218 suggest that the cultural adaptations at Xiamabei may reflect a first colonisation by modern  
219 humans, potentially involving cultural and genetic mixing with local Denisovans, and perhaps  
220 replaced by a later second arrival. This supports the view that current evolutionary scenarios are  
221 simplistic and that we should expect repeated but differential episodes of genetic and cultural  
222 exchange over large geographic areas. We should also expect to identify a mosaic pattern  
223 involving, in some instances, the spread of innovation packages, and in others, the persistence of  
224 local traditions or the adoption of local invention of innovations with different rates of  
225 complexities in technological and symbolic practices. This more complex evolutionary scenario  
226 fits better with current biological and cultural evidence in comparison to one that envisions a  
227 spread of innovation associated with a single, rapid wave of *H. sapiens* populations across  
228 Eurasia.

## 229 **References**



- 230 1. Bae, C. J., Douka, K. & Petraglia, M. On the origin of modern humans: Asian perspectives. *Science* **358**,  
231 1269–1269 (2017).
- 232 2. Fu, Q. et al. DNA analysis of an early modern human from Tianyuan Cave, China. *Proc. Natl. Acad. Sci. U.S.A.*  
233 **110**, 2223–2227 (2013).
- 234 3. Massilani, D. et al. Denisovan ancestry and population history of early East Asians. *Science* **370**, 579–583  
235 (2020).
- 236 4. Li, F., Bae, C. J., Ramsey, B., Chen, F. & Gao, X. Re-dating Zhoukoudian Upper Cave, northern China and its  
237 regional significance. *J. Hum. Evol.* **121**, 170–177 (2018).
- 238 5. Timmermann, A. & Friedrich, T. Late Pleistocene climate drivers of early human migration. *Nature* **538**, 92–95  
239 (2016).
- 240 6. Kuhlwilm, M. I. et al. Ancient gene flow from early modern humans into Eastern Neanderthals. *Nature* **530**,  
241 429–433 (2016).
- 242 7. Bae, C. J. et al. Late Pleistocene human evolution in Eastern Asia behavioral perspectives. *Curr. Anthropol.* **58**,  
243 514–526 (2017).
- 244 8. Hajdinjak, M. et al. Initial Upper Palaeolithic humans in Europe had recent Neanderthal ancestry. *Nature* **592**,  
245 253–257 (2021).
- 246 9. Bar-Yosef, O. & Wang, Y. Palaeolithic Archaeology in China. *Annu. Rev. Anthropol.* **41**, 319–335 (2012).
- 247 10. Li, F., Petraglia, M., Roberts, P. & Gao, X. The northern dispersal of early modern humans in eastern Eurasia.  
248 *Chin. Sci. Bull.* **65**, 1699–1701 (2020).
- 249 11. Dennell, R., Martínón-Torres, M., de Castro, J. M. B. & Gao, X. A demographic history of late Pleistocene  
250 China. *Quat. Int.* **559**, 4–13 (2020).
- 251 12. deMenocal, P. B. & Stringer, C. Climate and the peopling of the world. *Nature* **538**, 49–50 (2016).
- 252 13. Harvati, K. et al. Apidima Cave fossils provide earliest evidence of *Homo sapiens* in Eurasia. *Nature* **571**,  
253 500–504 (2019).
- 254 14. Dennell, R. *From Arabia to the Pacific: How Our Species Colonised Asia* (Routledge, London, ed. 1, 2020).
- 255 15. Hovers, E., Ilani, S., Bar-Yosef, O. & Vandermeersch, B. An early case of color symbolism: ochre use by  
256 modern humans in Qafzeh Cave. *Curr. Anthropol.* **44**, 491–522 (2003).
- 257 16. Watts, I. Red ochre, body painting, and language: interpreting the Blombos ochre. *The Cradle of Language* **2**,  
258 93–129 (2009).
- 259 17. Zipkin, A. M. *Material Symbolism and Ochre Exploitation in Middle Stone Age East-Central Africa* (Doctoral  
260 dissertation, The George Washington University, 2015).
- 261 18. Villa, P. et al. Border Cave and the beginning of the Later Stone Age in South Africa. *Proc. Natl. Acad. Sci.*  
262 *U.S.A.* **109**, 13208–13213 (2012).
- 263 19. Pargeter, J. & Shea, J. Going big versus going small: Lithic miniaturization in hominin lithic technology. *Evol.*  
264 *Anthropol.* **28**, 72–85 (2019).
- 265 20. Zwyns, N. et al. The northern route for human dispersal in central and Northeast Asia: New evidence from the  
266 site of Tolbor-16, Mongolia. *Sci. Rep.* **9**, 11759 (2019).
- 267 21. Peng, F., Lin, S. C., Patania, I. & Levchenko, V. A chronological model for the Late Paleolithic at Shuidonggou  
268 Locality 2, North China. *PLoS ONE* **15**, e023268 (2020).
- 269 22. Li, F. et al. The easternmost Middle Paleolithic (Mousterian) from Jinsitai Cave, North China. *J. Hum. Evol.*  
270 **114**, 76–84 (2018).
- 271 23. Li, F. et al. Chronology and techno-typology of the Upper Palaeolithic sequence in the Shuidonggou area,  
272 northern China. *J. World Prehistory* **32**, 111–141 (2019).
- 273 24. Yue, J. et al. Human adaptations during MIS 2: Evidence from microblade industries of Northeast China.  
274 *Palaeogeogr. Palaeoclimatol. Palaeoecol.* **567**, 110286 (2021).
- 275 25. Li, Z., Doyon, L., Li, H., Wang, Q. & d’Errico, F. Engraved bones from the archaic hominin site of Lingjing,  
276 Henan Province. *Antiquity* **93**, 886–900 (2019).
- 277 26. Wei, Y., d’Errico, F., Vanhaeren, M., Peng, F. & Gao, X. A technological and morphological study of Late  
278 Paleolithic ostrich eggshell beads from Shuidonggou, North China. *J. Archaeol. Sci.* **85**, 83–104 (2017).
- 279 27. Qu, T., Bar-Yosef, O., Wang, Y. & Wu, X. The Chinese Upper Paleolithic: Geography, Chronology, and  
280 Techno-typology. *J. Archaeol. Res.* **21**, 1–73 (2013).
- 281 28. Martí, A. P., Wei, Y., Gao, X., Chen, F. & d’Errico, F. The earliest evidence of coloured ornaments in China:  
282 The ochred ostrich eggshell beads from Shuidonggou Locality 2. *J. Anthropol. Archaeol.* **48**, 102–113 (2017).
- 283 29. Guan, Y. et al. Microblade remains from the Xishahe site, North China and their implications for the origin of  
284 microblade technology in Northeast Asia. *Quat. Int.* **535**, 38–47 (2020).

- 285 30. Pargeter, J. & Faith, T. J. Lithic miniaturization as adaptive strategy: a case study from Boomplaas Cave, South  
286 Africa. *Archaeol. Anthropol. Sci.* **12**, 225 (2020).  
287 31. Guo, Y. J. et al. Luminescence ages for three ‘Middle Paleolithic’ sites in the Nihewan Basin, northern China,  
288 and their archaeological and palaeoenvironmental implications. *Quat. Res.* **85**, 456–470 (2016).  
289 32. Yang, S., Deng, C., Zhu, R. & Petraglia, M. The Paleolithic in the Nihewan Basin, China: Evolutionary history  
290 of an Early to Late Pleistocene record in Eastern Asia. *Evol. Anthropol.* **29**, 125–142 (2020).  
291 33. Scerri, E., Chikhi, L. & Thomas, M. Beyond multiregional and simple out-of-Africa models of human evolution.  
292 *Nat. Ecol. Evol.* **3**, 1–3 (2019).  
293

## 294 **Acknowledgements**

295 We thank Y. Lefrais (IRAMAT-CRP2A, UMR 5060 CNRS CNRS – Université Bordeaux-  
296 Montaigne, France) and F. Orange (Université Côte d’Azur, Centre Commun de Microscopie  
297 Appliquée, CCMA, Nice, France) for assistance with SEM-EDS analyses; A. Queffelec (PACEA  
298 UMR 5199, University Bordeaux, CNRS, France) and L. Geis (PACEA UMR 5199, University  
299 Bordeaux, CNRS, France) for assistance with the EDXRF analyses and the 3D imaging; C. X.  
300 Zhang, B. Hu, M. L. Zhou, J. H. Li, Y. Liu, S. H. Yang, X. G. Li, Y. Chen, J. Yuan, Z. S. Shen,  
301 S. Zhang and Z. X. Jiang (Institute of Geology and Geophysics, Chinese Academy of Sciences)  
302 for assistance with the sediment analysis; B. Xu (Institute of Geology and Geophysics, Chinese  
303 Academy of Sciences) and Y. Li (China University of Geosciences, Beijing) for discussions on  
304 dating results; and R. P. Tang and F. X. Huan (Institute of Vertebrate Palaeontology and  
305 Palaeoanthropology, Chinese Academy of Sciences) for assistance with figure preparation.

306 **Funding** Financial support for this research was provided by the National Natural Science  
307 Foundation of China (41888101, 42177424, 41977380, 42072212 and 41690112), the Strategic  
308 Priority Research Program of Chinese Academy of Sciences (XDB26000000), the Key Research  
309 Program of the Institute of Geology & Geophysics, Chinese Academy of Sciences (IGGCAS-  
310 201905), the State Key Laboratory of Loess and Quaternary Geology, Institute of Earth  
311 Environment (SKLLQGZR2002), the Youth Innovation Promotion Association of Chinese  
312 Academy of Sciences (2020074), the Humboldt Foundation, and the Max Planck Society. O.A.  
313 was supported by the Spanish MICIU/Feder (PGC2018-093925-B-C32), the Catalan AGAUR  
314 (SGR2017-1040) and the Univ. Rovira i Virgili (2019-PFR-URV-91) in the context of a MICIN  
315 “María de Maeztu” excellence accreditation (CEX2019-000945). D.E.R. was funded by the  
316 Fyssen Foundation, France, and the Juan de la Cierva-Formación Research Fellowship  
317 (FJC2018-035605-I; Ministerio de Ciencia e Innovación, Spain). F.D. was funded by the  
318 Research Council of Norway through its Centre of Excellence funding scheme (SFF Centre for  
319 Early Sapiens Behaviour –SapienCE– project number 262618), the Talents program and the  
320 GPR Human Past of the University of Bordeaux Initiative of Excellence. KD has received  
321 funding from the ERC under the European Union’s Horizon 2020 research and innovation  
322 program, grant agreement 715069-FINDER-ERC-2016-STG.

323 **Author contributions** F.G.W., S.X.Y., C.L.D, R.X.Z., Z.T.G., F.D.E. and M.P. obtained  
324 funding and initiated the project; F.G.W., S.X.Y., J.Y.G, L.Q.L., F.X., Y. H.Y., Y.G. and W.Y.L.

325 conducted field excavation and site sampling; J.Y.G., K.L.Z., K.D. and C.L.D. conducted  
326 stratigraphic and palaeoenvironmental studies; J.Y.G. performed the OSL dating; K.D.  
327 performed the <sup>14</sup>C dating; S.X.Y., J.P.Y., M.P. and A.O. analyzed the stone artefacts; F.D.E.,  
328 D.E.R., Y.G. and C.L.D. analyzed the ochre processing artefacts and the sediment; and S.X.Y.,  
329 C.L.D, F.D.E. and M.P wrote the main text and supplementary materials with specialist  
330 contributions from the other authors.

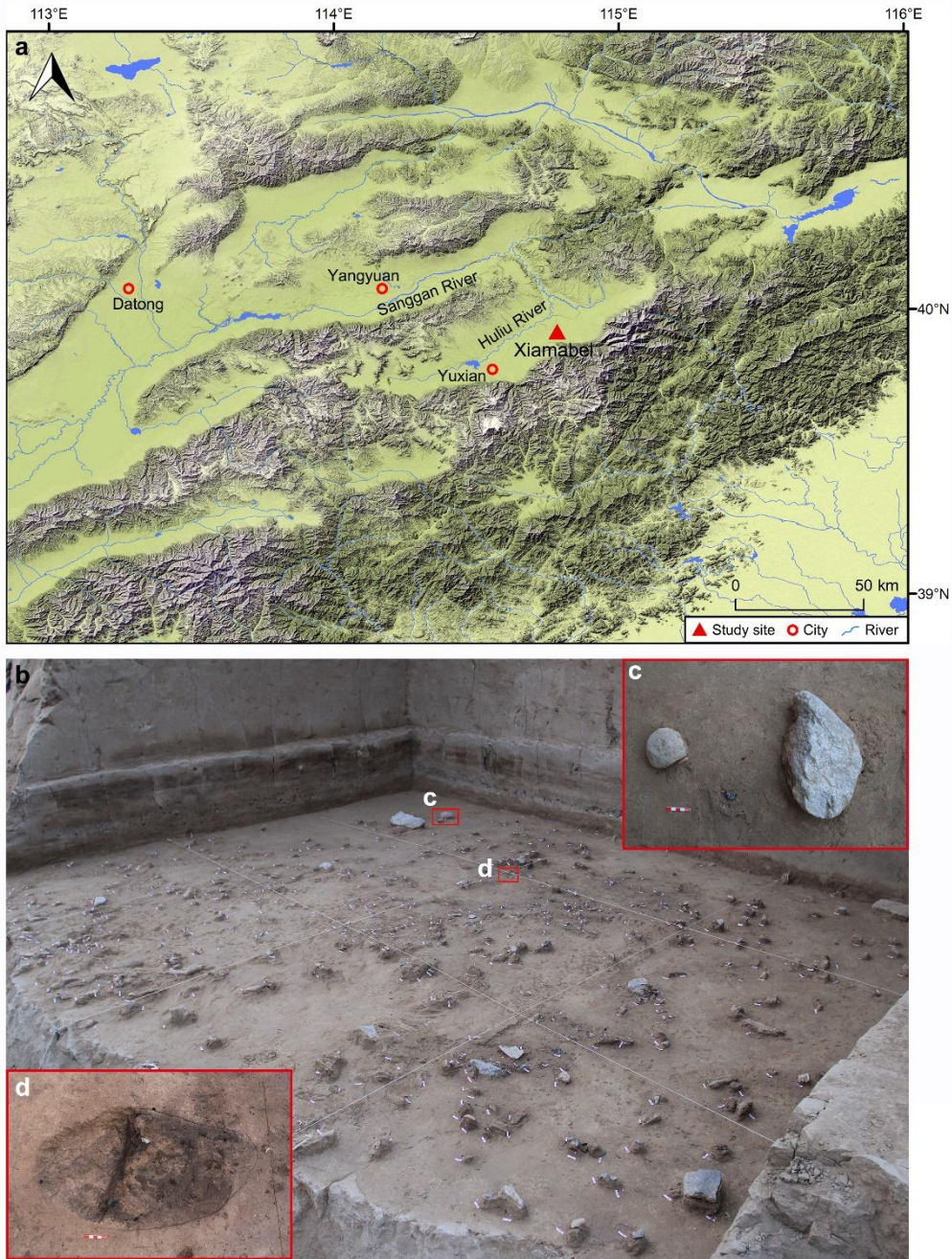
331 **Competing interests** The authors declare no competing interests.

332 **Data and materials availability** All relevant data are available in the main text or the  
333 accompanying supplementary materials. All artefacts referred to in this study are curated in the  
334 Institute of Vertebrate Palaeontology and Palaeoanthropology, Chinese Academy of Sciences,  
335 Beijing, and Hebei Provincial Institute of Cultural Relics and Archeology in Shijiazhuang, China.  
336 They are available for further research.

### 337 **Supplementary Materials**

338 Supplementary Information A–I

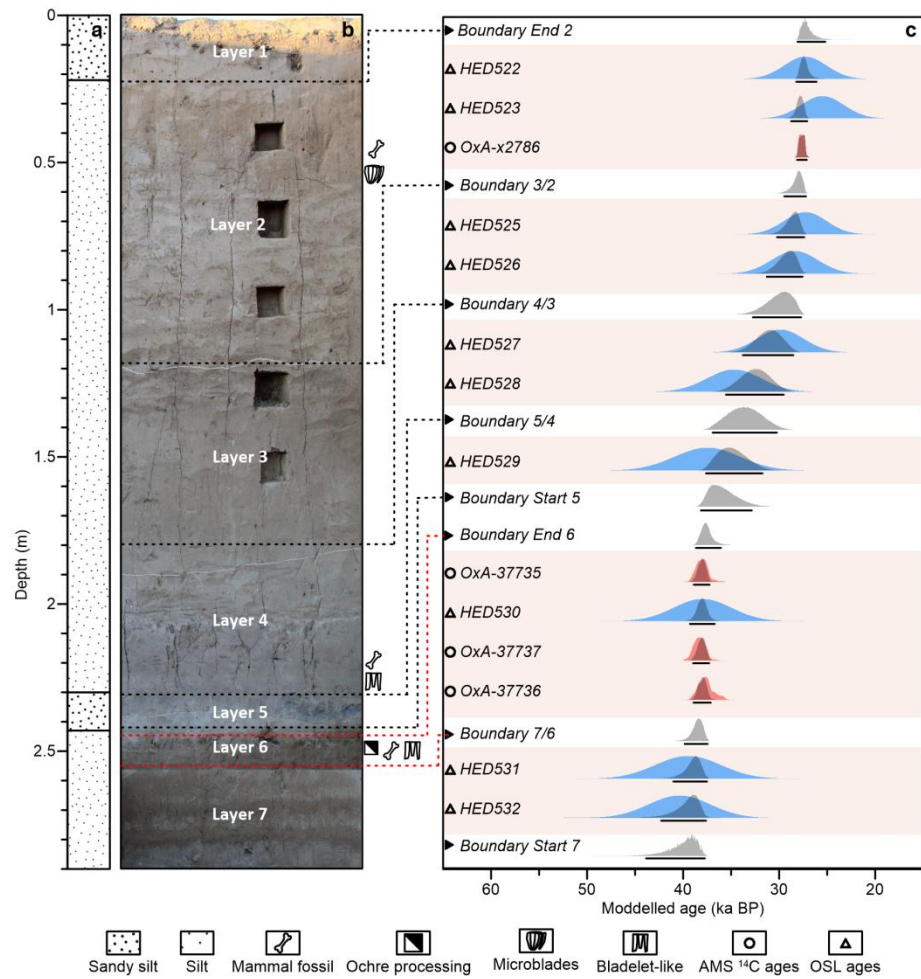
339 SI References



340

341 **Fig. 1 | Location of Xiamabei in the Nihewan Basin, China, and archaeological site**  
 342 **excavations.** **a**, Location of Xiamabei in northern China, with regional map showing the  
 343 location of the site on the south bank of the Huli River, Nihewan Basin. **b**, Distribution of  
 344 cultural remains on the Layer 6 surface. **c**, Ochre processing feature showing a quartzite cobble  
 345 (QC), an ochre piece (OP1) and a limestone slab (LS). **d**, View of the Layer 6 hearth, dated to  
 346 ~41–39 ka.

347



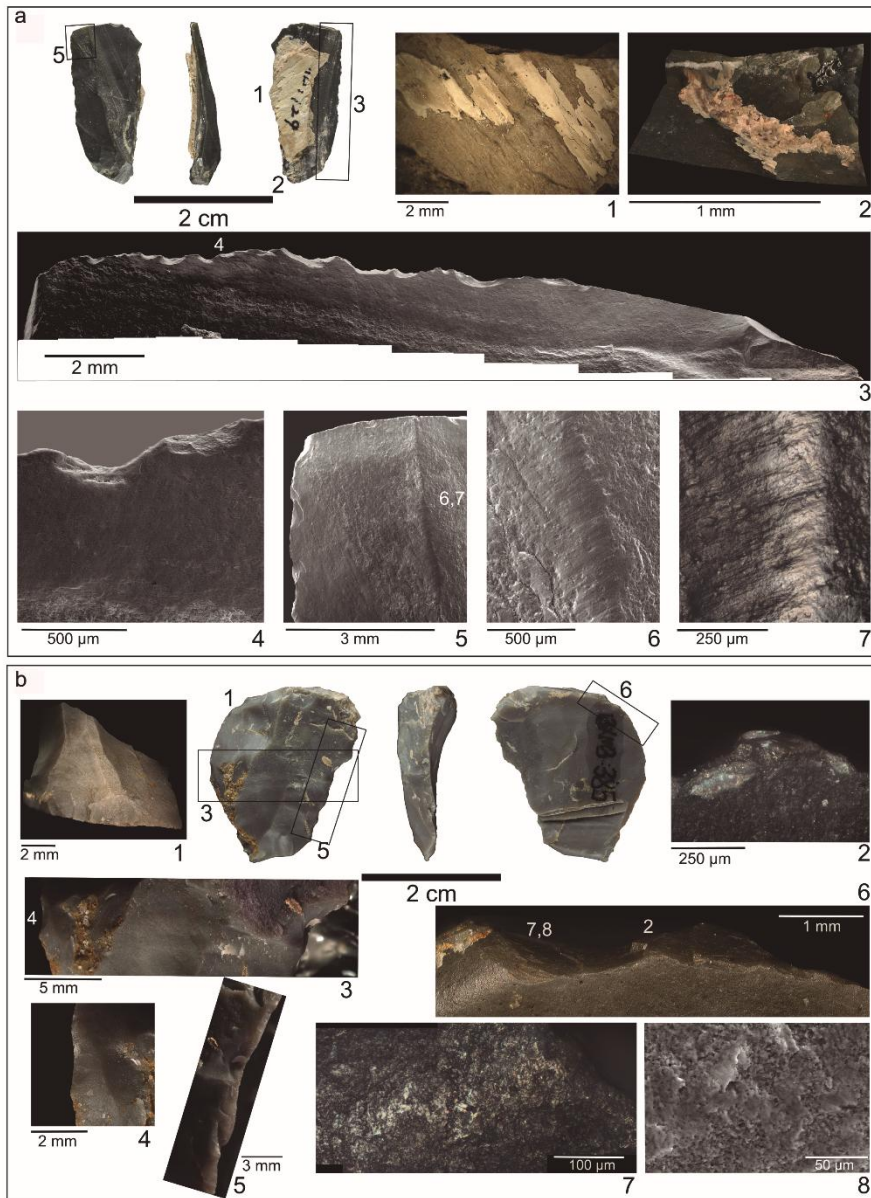
348

349 **Fig. 2 | Stratigraphy, sedimentary sequence and the position of luminescence and**  
 350 **radiocarbon samples at Xiamabei. a, Main stratigraphic column. b, Layers identified in the**  
 351 **field. c, Bayesian model of AMS <sup>14</sup>C and OSL dates. The age probability distribution in blue, red**  
 352 **and gray correspond to the OSL, AMS <sup>14</sup>C and modelled ages, respectively.**



353

354 **Fig. 3 | Artefacts laying on the red stained sediment patch.** **a**, Quartzite cobble (QC),  
 355 limestone slab (LS) and ochre piece (OP1) identified during the excavation. **b**, LS laying on an  
 356 intense red stained sediment patch. **c**, Ochre piece modified by grinding (OP1). **d**, Ochre  
 357 fragment probably resulting from crushing a larger ochre piece (OP2). **e**, LS showing ochre  
 358 staining. **f**, Ochre microfragment (OMF) collected on the LS. **g**, Quartzite cobble (CG).



359

360 **Fig. 4 | Examples of use wear on lithics and residues on hafted pieces. a,** Bladelet-like piece  
 361 with an adhering portion of the bone haft (no. 129); (1) detail of the bone; (2) imprints of plant  
 362 fibers on calcium carbonate concretions likely related to binding; (3) ventral view of the active  
 363 edge; (4-7) several details of the grit-influenced plant polish produced by a whittling action. **b,**  
 364 End-scraper with punctual distal retouch (no. 385); (1) frontal view of the retouched area; (2)  
 365 spot with ochre particles on the active distal end; (3-5) scarring and slight adequation on the  
 366 hafted portion; (6-8) use wear produced by hide scraping. Images: a1-2 and b1, 3-6 3D Digital  
 367 Microscope; a3-6, b8 Scanning Electron Microscope; a7, b2, 7 Reflected Light Optical  
 368 Microscope.

## 369 **Methods**

### 370 **Radiocarbon dating**

371 Six animal bone fragments (all mammals) from Layers 2, 4 and 6 were collected and submitted  
372 to the Oxford Radiocarbon Accelerator Unit (ORAU) for radiocarbon dating. The bones were  
373 pretreated using routine methods for collagen extraction and purification, including an  
374 ultrafiltration step, as described in Ramsey et al.<sup>34</sup> and Brock et al.<sup>34</sup>.

375 The dates are reported in radiocarbon years BP (Before Present - AD 1950) using the half-  
376 life of 5568 years. Isotopic fractionation was corrected for using the  $\delta^{13}\text{C}$  values measured on the  
377 AMS. The quoted  $\delta^{13}\text{C}$  values are measured independently on a stable isotope mass spectrometer  
378 (to  $\pm 0.3$  per mil relative to VPDB). The new  $^{14}\text{C}$  determinations are calibrated using the  
379 INTCAL20 calibration curve<sup>36</sup> and the OxCal 4.4 platform<sup>37</sup>, with the age ranges in  
380 Supplementary Information Table C1 expressed at the 95.4% confidence interval. The dating  
381 report is included in Supplementary Information C1.

### 382 **Luminescence dating**

383 Dating of sediments using optically stimulated luminescence (OSL) signals in mineral grains was  
384 first introduced by Huntley et al.<sup>38</sup>. The OSL dating technique mostly determines the time  
385 elapsed since the last sunlight exposure of a deposit, i.e., its burial time. The technique has been  
386 widely used to date geological and archaeological deposits<sup>39-42</sup> in recent decades. The  
387 luminescence emitted from minerals (e.g., quartz and feldspar) under artificial light exposure is  
388 proportional to the absorbed energy accumulated within the crystal lattice of minerals by ionizing  
389 radiation (e.g., alpha, beta or gamma radiation) from radioactive elements such as uranium (U),  
390 thorium (Th), and potassium (K) in the environment, as well as cosmic rays<sup>40,43</sup>. The total  
391 luminescence of a sample which is often calibrated as a radiation dose (termed the equivalent  
392 dose, De), is determined by comparing natural luminescence signals with signals yielded after a  
393 known laboratory irradiation dose. Calculating the rate of natural irradiation (dose rate) at which  
394 the sample absorbs energy from radiation in the environment during burial involves assessing the  
395 radioactivity of the sample and its surroundings using chemical and radiometric methods, and  
396 estimating the radiation contributed by cosmic rays. The luminescence age of sediments is then



397 achieved by subdividing the equivalent dose (Gy) by the dose rate (Gy/ka)<sup>44</sup>.

398 A total of 10 sediment samples (Supplementary Information Table C3) was collected in the  
399 Xiamabei sequence for OSL dating. All OSL samples were obtained by hammering steel tubes  
400 (20 cm-long cylinders with a diameter of 5 cm) into a freshly dug vertical section. The tubes  
401 were then covered and sealed with aluminum foil, and wrapped in black plastic bags and taped to  
402 avoid light exposure and moisture loss. The sediment from the sunlight-exposed end of the  
403 cylinder was separated and used for dose rate measurement. The material from the middle of the  
404 cylinder was used for De measurement. Sample preparation, measurement and data analysis  
405 procedures are described in Supplementary Information C2.

### 406 **Bayesian modelling and age of the Xiamabei section**

407 To establish the precise chronological framework of individual depositional units in Xiamabei,  
408 we conducted Bayesian analysis that includes both the optical and <sup>14</sup>C ages, using OxCal v4.4  
409 <sup>45–49</sup>. All <sup>14</sup>C ages were calibrated using the INTCAL 20 calibration curve. For each OSL age, we  
410 used C date in calendar years before 2020 when the samples were collected with associated 1σ  
411 errors as likelihood estimates. In order to harmonise the time the OSL was obtained and the  
412 radiocarbon convention “BP=1950”, we subtracted 70 years from the OSL ages (2020–1950)  
413 prior to them being modeled.

414 In order to estimate the posterior distributions (i.e., the modelled ages), the stratigraphic  
415 order of each sample was input using the Sequence function (Supplementary Information Table  
416 C4), based on the prior assumption that a sample stratigraphically lower is older than those above.  
417 Samples that are from the same stratigraphic layer with similar depth, such as in Layer 6, were  
418 modelled as a Phase, in which the measured ages are assumed to belong to same period. For the  
419 layers with abrupt and clear boundaries between them, such as Layers 6 and 5, double (upper or  
420 lower) boundaries were placed for them to constrain their start or end ages. Otherwise, for layers  
421 which gradual stratigraphic changes were identified, assuming continuous sediment  
422 accumulation, single transitional boundaries were placed between them. The samples, phases and  
423 sequences were arranged according to their relative stratigraphic order.

424 To check for outliers, we applied the general t-type outlier model to detect outlier ages by  
425 assessing the likelihood of each age being consistent with the modelled ages. A prior outlier  
426 probability of 5% was assigned for the other samples with their posterior outlier probability

427 calculated during the modelling process. The CQL codes used to run the Bayesian model and  
428 generate posterior age estimates are listed in Supplementary Information Table C5. The  
429 generated probability distribution functions (PDF) for each of the samples are shown in Fig. 2  
430 and their corresponding 95.4% probability ranges are summarized in Supplementary Information  
431 Table C5. As demonstrated in Fig. 2, the Bayesian model results in a significant improvement of  
432 the precision in age estimates for all the samples. None of the samples was flagged as an outlier,  
433 as indicated by the posterior outlier probabilities, which are less than 4% for all samples. Using a  
434 Date command we calculated the total span of each phase of interest, in particular, Layer 6 and  
435 Layer 4. The model is shown in Supplementary Information C3.

### 436 **Ochre analysis**

437 Four artefacts were submitted to microscopic and geochemical analyses (Fig. 3): two ochre  
438 pieces (OP1 and OP2, Extended Data Figs. 2,3), a quartzite cobble (QC, Extended Data Fig. 4)  
439 and an elongated limestone slab (LS, Extended Data Fig. 5). During excavation, these four  
440 artefacts were found in close spatial association (Fig. 3a) and lying on a large red stained  
441 sediment spot (Fig. 3b). The cobble was cleaned under the microscope with a wet toothpick and  
442 a soft brush. The recovered sediment was analysed to check the presence of phytoliths  
443 (Supplementary Information F).

444 The four artefacts were examined with a motorised Leica Z6APOA microscope equipped  
445 with a DFC420 digital camera and Leica Application Suite software (v.4.13, Wetzlar, Germany),  
446 equipped with the Multifocus module and Leica Map DCM 3D computer software (6.2, Wetzlar,  
447 Germany). The Multifocus module allows the acquisition of extended depth of field images by  
448 relying on adapted algorithms that combine digital images collected at different heights into a  
449 single, sharp, composite image. The obtained microscopic images were digitized and edited in  
450 the Adobe® Photoshop® CS5.1 Extended software. The Leica Map DCM 3D allowed  
451 production of 3D reconstructions of areas of interest on OP1.

452 Anthropogenic modifications on grindstones and ochre pieces were identified macro- and  
453 microscopically. On grindstones, we recorded the presence of pits (depressions produced by a  
454 pounding action), and smoothed areas (surfaces that have lost, comparatively to neighbouring  
455 areas, irregularities and projections through abrasive action)<sup>50-52</sup>. On ochre pieces, we identified  
456 polished areas (shiny surfaces that may have been produced by use or by rubbing against a soft

457 surface), striations (linear parallel marks arranged in groups produced by grinding the piece  
458 against an abrasive surface), and facets (flat areas covered with striations produced by grinding  
459 an object on a flat, hard abrasive surface)<sup>53–55</sup>.

460 An ochre microfragment (OMF, Fig. 3f; Extended Data Fig. 5) adhering to the surface of  
461 the limestone slab LS (zone 1 in Extended Data Fig. 5a) was removed with a scalpel under the  
462 microscope without producing any damage to the artefact and put on a carbon adhesive tab  
463 adhering to a SEM stub.

464 Scanning Electron Microscopy (SEM) observations and Energy Dispersive X-Ray  
465 spectroscopy (EDS) analyses on OP1 and OP2 were conducted with a JEOL IT 500 HR  
466 instrument equipped with two EDS Oxford Instruments Ultimex 100 spectrometers. Both  
467 samples were observed under the same magnifications ( $\times 60$ ,  $\times 1000$ ,  $\times 3000$ ,  $\times 4000$  and in a few  
468 cases  $\times 10,000$ ) (Supplementary Information E). EDS analyses and backscattered electron images  
469 (BSE) were obtained under low vacuum mode at a pressure of 30 Pa with a 20 kV accelerating  
470 voltage. SEM observations and EDS analyses on sample OMF were conducted with a Tescan  
471 Vega3 XMU scanning electron microscope (TESCAN FRANCE, Fuveau, France) equipped with  
472 an Oxford X-MaxN 50 EDS detector (Oxford Instruments, Abingdon, U.K). A 10 kV  
473 accelerating voltage was used for imaging using secondary and backscattered electrons, and 20  
474 kV for EDS analyses. All samples were observed with no prior metal or carbon coating. All EDS  
475 spectra were processed with the Aztec software (version 3.1, Oxford Instruments, UK).

476  $\mu$ -Raman ( $\mu$ -RS) analyses were conducted to determine the mineralogical composition of  
477 OP1, OP2 and sample OMF, using a SENTERRA Dispersive Raman Microscope (Bruker)  
478 equipped with an internal calibration system. The working area was examined using an  
479 integrated colour camera. Spectra were acquired with a 785 nm laser and a laser power of 1 to 10  
480 mW. The spectra were recorded with an integration time varying from 5 to 10 s, in a spectral  
481 range from 100 to 2200  $\text{cm}^{-1}$ , with a number of co-additions varying between 5 to 10 depending  
482 on the presence of fluorescence radiation and signal-to-noise ratio. Data was collected with the  
483 OPUS 7.2 software package (Bruker, Billerica, USA). Mineral identification was based on the  
484 comparison of the recorded spectra with those of available in the RRUFF spectra library,  
485 University of Arizona<sup>56</sup>.

486 The elemental composition of OP1 and OP2 was established by energy dispersive X-ray  
487 fluorescence (EDXRF) (Extended Data Fig. 6). Measurements were acquired using a positioning

488 device consisting of a metallic receptacle to which the spectrometer was fixed. Sample OMF was  
489 not analysed because its size is smaller than the spectrometer aperture (3x4 mm in diameter)<sup>57</sup>.  
490 EDXRF measurements were performed with a portable SPECTRO xSORT X-ray fluorescence  
491 spectrometer from Ametek, equipped with a silicon drift detector (SDD), a W X-ray tube with an  
492 excitation source set at 40 kV, 0.1 mA. Spectra acquisition times were set to 120 s. The  
493 spectrometer is internally calibrated by an automated measure of the elemental composition of a  
494 standard metal shutter. A supplementary calibration<sup>58,59</sup>, based on the Lucas-Tooth and Price  
495 methodology, was applied<sup>60</sup>. This calibration, developed with the X-labpro software (Ametek,  
496 Berwyn, USA) adjusts the mass attenuation coefficient and calibration slopes for major and trace  
497 elements by using certified standards and reference samples analysed by ICP-OES and ICP-MS.  
498 The Ochre analysis results in details can be found in Supplementary Information E.

#### 499 **Sediment analysis**

500 Twelve sediment samples, as listed in Supplementary Information Table G1, were selected for  
501 mineralogical, elemental and magnetic analysis. Two samples (X1 and X2) come from the red  
502 stained area on which the ochre fragments OP1 and OPI2, limestone slab LS and cobble QS were  
503 found (Extended Data Fig. 10), two samples (X3 and X6) were retrieved in the same layer but at  
504 ca. 2 m far from the stained area, eight other (X4, X5, XMB2101–XMB2106) were collected  
505 between 20 and 200 m far from the excavated area (Supplementary Information Fig. G1). All the  
506 samples consist of floodplain silt.

507 XRD analysis<sup>61</sup> was carried out on the twelve samples (Supplementary Information Table  
508 G1), using a Netherland PANalytical X'PerPRO diffractometer with the following parameters:  
509 Ni-filtered Cu-K $\alpha$ /40kV/40mA, scattering slit of 1/16°, receiving slit of 5 mm, continuous scan  
510 mode, scanning speed of 0.049884°/s, and a scanning step of 0.0167113°. Bulk minerals were  
511 identified based on the following peaks: quartz, 4.26 Å; anorthoclase, 3.21 Å; albite, 3.18 Å;  
512 rutile, 3.189 Å; calcite, 3.03 Å; dolomite, 2.89 Å; Hematite, 2.70 Å; Koninckite, 8.42 Å; and clay  
513 minerals smectite/chlorite, 14.1 Å; illite, 10.0 Å. The relative proportions of the identified  
514 minerals were roughly determined using their peak intensities by measuring the heights of the  
515 main reflections with PANalytical X'pert HighScore software (Version 2.2e).

516 Raman spectra<sup>61,62</sup> were obtained with a Witec alpha300R confocal-Raman spectrometer  
517 equipped with a solid-state continuous-wave laser emitting at 532 nm, and diffraction gratings of

518 300 grooves  $\text{mm}^{-1}$ . A piece of single-crystal silicon was used to calibrate the wavenumbers of  
519 the shifts. Laser focusing and sample viewing are performed through a Zeiss microscope fitted  
520 with an EC Epiplan 50 $\times$  objective lens (NA=0.75). The spot size is less than 1  $\mu\text{m}$  and the  
521 resolution is 4.8  $\text{cm}^{-1}$ . The laser power impinging on the hematite single crystal was 0.40 mW. A  
522 spectra acquisition time of 30 s and total spectra with 20 accumulations were collected for each  
523 measurement.

524 Non-destructive Micro-XRF analyses were performed on the twelve sediment samples  
525 (Supplementary Information Table G1) following the procedures of Li et al.<sup>63</sup>. The Micro-XRF  
526 measurements were carried out on the M4 TORADO PLUS Micro-XRF analyzer. One area of  
527 about 0.5–1  $\text{cm}^2$  for each sample was randomly selected for collecting the XRF signals with the  
528 same measuring parameters (e.g., 50 kV of high voltage, 600  $\mu\text{A}$  of anode current, 20  $\mu\text{m}$  of spot  
529 size, 10  $\mu\text{m}$  of pixel size, and 20 ms/pixel of pixel time). For semi-quantitative comparisons,  
530 each XRF spectrum was normalized with the signal of the Rh-La peak, which is generated by a  
531 Rh X-ray source. The data were analyzed with the M4 TORNADO Bruker Microanalysis  
532 Software.

533 Mineral magnetic measurements were made on the twelve sediment samples  
534 (Supplementary Information Table G1) in order to determine the magnetic mineralogy<sup>64–71</sup>.  $\chi$ - $T$   
535 curves were obtained by continuous exposure of samples through temperature cycles from room  
536 temperature to 700°C and back to room temperature with a ramping rate of 2°C/min, using an  
537 AGICO MFK1-FA equipped with CS-3 temperature control system. To minimize the possibility  
538 of oxidation, the samples were heated and cooled in an argon atmosphere. For each sample, we  
539 subtracted the contribution of the sample holder and thermocouple to the magnetic susceptibility.  
540 Hysteresis loops were measured using a MicroMag 3900 Vibrating Sample Magnetometer (VSM)  
541 (Princeton Measurements Corp., USA). The magnetic field was cycled between  $\pm 1.5$  T for each  
542 sample. Saturation magnetization ( $M_s$ ), saturation remanence ( $M_r$ ), and coercivity ( $B_c$ ) were  
543 determined after the correction for the paramagnetic contribution identified from the slope at  
544 high fields. Samples were then demagnetized in alternating fields up to 1.5 T, and an isothermal  
545 remanent magnetization (IRM) was imparted from 0 to 1.5 T also using the MicroMag 3900  
546 VSM. Subsequently the IRM at 1.5 T was demagnetized in a stepwise backfield from 0 to  $-1.5$  T  
547 to obtain coercivity of remanence ( $B_{cr}$ ). Magnetic component analyses of coercivity distributions  
548 were analyzed using the IRM-CLG program of Kruiver et al.<sup>66</sup>.

549 To better constrain the origin and microstructure of the sediment, selected samples (X1, X2,  
550 X4, X6) were observed using optical microscopy and analysed using Scanning Electron  
551 Microscopy (SEM) coupled with Energy Dispersive X-Ray spectroscopy (EDS). Backscattered  
552 electron microscopy analyses were conducted using a scanning electron microscope with an  
553 energy dispersive spectrometer (JSM-IT500).

554 Detailed results of the sediment analyses can be found in Supplementary Information G.

555

## 556 **Stone tool functional and residue analysis**

557 The stone tool functional analysis is based on the fundamentals of traceology<sup>72-74</sup>, which has  
558 been subsequently consolidated, systematized<sup>75-79</sup> and strengthened to improve interpretation<sup>76,77</sup>.  
559 The study applied criteria established experimentally<sup>80-84</sup>, incorporating a multi-scalar approach  
560 and a multi-technique microscopic analysis<sup>75-88</sup>. Potential residues were characterized  
561 microscopically, including study of their elementary chemical composition, without removing  
562 adhering materials from tools<sup>89-92</sup>.

563 Use-wear and residues were documented with the combined use of Optical Microscopy  
564 (OM), Scanning Electron Microscopy (SEM) and 3D Digital Microscopy (3D DM). Four main  
565 procedures (I-IV) were used for analysis.

566 I) A preliminary assessment of the samples and the location of features of special interest  
567 was conducted. This was conducted at low magnification, using a stereomicroscope (Euromex  
568 DZ.1105), with a magnification range of 8×-80× (0.8×-8× zoom, 10× oculars), and equipped  
569 with a 20MP 1” Scemex camera (Horizontal Field of View 16.6 mm -1.67 mm).

570 II) A systematic screening at different magnifications using 3D DM (Hirox KH-8700) was  
571 conducted. This microscope is equipped with a dual illumination revolver zoom lens (MXG-  
572 5000REZ) which together with the high intensity LED light source allows for the observation of  
573 samples with a 5700 K color temperature. This lens consists of a triple objective turret with a  
574 different zoom range per objective, allowing for magnifications ranging from 35 to 5000×  
575 (HFOV 8.6 mm–60 μ). The microscope is equipped with a high-sensitivity compact CCD camera  
576 that enabled the capture of 24 frames per second at high resolution (1600×1200 pixels). The dual  
577 illumination system allows for the observation of sample topography with ring and coaxial light.

578 The former is suitable for the observation of topographical irregularities with a uniform even  
579 illumination at low magnifications, while coaxial light serves to highlight the topography of flat  
580 surfaces at high magnifications. Ring and coaxial lights were used individually and even  
581 combined, according to the observation conditions required by the samples. The interest of this  
582 microscope lies on its integrated stacking and stitching technology, capable of performing real-  
583 time 2D and 3D tiltings and generating wide field of view images of large surface areas which, in  
584 turn, create quantifiable 3D models.

585 III) More conventional observations were conducted with a reflected light microscope. We  
586 used a Zeiss Axio Scope A.1 metallographic microscope, with differential interference contrast  
587 (DIC) system involving a Nomarsky interference contrast filter. The microscope was equipped  
588 with 10× oculars and objectives EC Epiplan ranging from 5×/0.13 to 50×/0.5 HD DIC, resulting  
589 in nominal magnifications ranging from 50 to 500 times. Pictures were taken with a 6.3 MP 1.8”  
590 FLIR camera, and fully focused images were obtained through a motorized stage and Winkoms  
591 Encoder Z 1.0 and Helicon Focus 5.3 software. Resulting HFOV ranges from 2.9mm to 295µm.

592 IV) An environmental SEM (ESEM FEI Quanta 600 model) with an energy dispersive X-  
593 ray spectrometer (EDX-EXL II System analytical oxford) for microanalysis, equipped with an  
594 INCA software (v 4.01) from Oxford Instruments for digital image acquisition, was conducted.  
595 Most observations were carried out between 60× and 2000× (HFOV 6.9 mm to 207 µ, 24”  
596 display). Observations were entirely done in low vacuum mode (LV), so the coating of the  
597 samples with conductive materials (gold or carbon) was not required. Large field (LFD) and  
598 back-scattered electron detectors (DualBSD) were used in combination to observe residues and  
599 use-wear features.

600 Sample processing based on protocols tested in previous studies<sup>79,87</sup> were adapted in our  
601 microscopic workflow. No cleaning was applied during first observations; a very soft cleaning  
602 was performed prior to the characterization of residues by OM, 3D DM or SEM analysis; and, a  
603 more thorough cleaning was subsequently applied when necessary, to document use-wear  
604 features in detail. The main cleaning steps were: 1) Removal of the ink and varnish used to mark  
605 the archaeological tools with acetone; 2) 5 to 15 min ultrasonic baths in a 2% neutral phosphate-  
606 free detergent solution (Derquim®); 3) 5 min baths in hydrogen peroxide (H<sub>2</sub>O<sub>2</sub>, 130vol) to  
607 remove modern organic matter, when spotted; 4) Removal of residues from cleaning products  
608 under running water; 5) 2–5 min ultrasonic baths in pure acetone to remove any residues from

609 handling. When necessary, 5 min baths in a 10% HCl solution were applied to remove  
610 carbonated residues. Before each observation, tools were dried with compressed air to avoid  
611 contact with the laboratory paper and to reduce the formation of liquid spots on the surface,  
612 which may lead to misleading interpretations. During the entire process, samples were handled  
613 using powder-free gloves and plastic tweezers.

614 Experimental reference collections available at the IPHES Lithic Technology Laboratory,  
615 derived from published and ongoing programs, were used to compare to the Xiamabei results,  
616 thereby assisting in interpretations. The experimental programs involved actions on a range of  
617 common contact materials, and artefacts made on a variety of raw materials, including chert,  
618 quartzite, quartz, limestone, basalt, and obsidian<sup>83–85,88,90,91,93–97</sup>. Interpretations were also  
619 supported by information supplied in the wider literature. Detailed reporting on the Xiamabei  
620 samples is provided in Supplementary Information I.

621

622

- 623 34. Ramsey, B. C., Higham, T. & Leach P. Towards high-precision AMS: Progress and limitations.  
624 *Radiocarbon* **46**, 17–24 (2004).
- 625 35. Brock, F., Higham, T., Ditchfield, P. & Ramsey C. B. Current pretreatment methods for AMS radiocarbon  
626 dating at the Oxford Radiocarbon Accelerator Unit (ORAU). *Radiocarbon* **52**, 103–112 (2010).
- 627 36. Reimer, P. et al. The IntCal20 Northern Hemisphere radiocarbon age calibration curve (0–55 cal kBP).  
628 *Radiocarbon* **62**, 725–757 (2020).
- 629 37. Bronk, C. B. Bayesian analysis of radiocarbon dates. *Radiocarbon* **51**, 337–360 (2009).
- 630 38. Huntley, D. J., Godfrey-Smith, D. I. & Thewalt, M. L. W. Optical dating of sediments. *Nature* **313**, 105–  
631 107 (1985).
- 632 39. Duller, G. Distinguishing quartz and feldspar in single grain luminescence measurements. *Radiat. Meas.*  
633 **37**, 161–165 (2003).
- 634 40. Rhodes, E. J. Optically stimulated luminescence dating of sediments over the past 200,000 years. *Annu.*  
635 *Rev. Earth Planet. Sci.* **39**, 461–488 (2011).
- 636 41. Zhang, X. L. et al. The earliest human occupation of the high-altitude Tibetan Plateau 40 thousand to 30  
637 thousand years ago. *Science* **362**, 1049–1051 (2018).
- 638 42. Ge, J. Y. et al. Evidence from the Dayao Palaeolithic site, Inner Mongolia for human migration into arid  
639 northwest China during mid-Pleistocene interglacials. *Quat. Res.* **103**, 113–129.
- 640 43. Duller, G. Luminescence dating of Quaternary sediments: Recent advances. *J. Quat. Sci.* **19**, 183–192  
641 (2004).
- 642 44. Aitken, M. J. *Introduction to Optical Dating: The Dating of Quaternary Sediments by the Use of Photon-*  
643 *Stimulated Luminescence* (Clarendon Press, 1998).
- 644 45. Ramsey, B. C. Deposition models for chronological records. *Quat. Sci. Rev.* **27**, 42–60 (2008).
- 645 46. Ramsey, B. C. Bayesian analysis of radiocarbon dates. *Radiocarbon* **51**, 337–360 (2009).
- 646 47. Ramsey, B. C. Dealing with outliers and offsets in radiocarbon dating. *Radiocarbon* **51**, 1023–1045 (2009).
- 647 48. Ramsey, B. C. *Bayesian Approaches to the Building of Archaeological Chronologies* (CRC Press Boca  
648 Raton, FL, 2015).
- 649 49. Ramsey, B. C. Methods for summarizing radiocarbon datasets. *Radiocarbon* **59**, 1809–1833 (2017).
- 650 50. Adams, J. et al. “Functional analysis of macro-lithic artefacts” in Non-Flint Raw Material Use in  
651 Prehistory: Old Prejudices and New Directions, F. Sternke, L. Eigeland, L.J. Costa, Eds. (Archaeopress,



- 2009), pp. 43–66.
- 653 51. de Beaune, S. *Pour une archéologie du geste: Broyer, moudre, piler, des premiers chasseurs aux premiers*  
654 *agriculteurs* (CNRS Editions, 2000).
  - 655 52. Rosso, D. E., Mart, í A. P. & d’ Errico, F. Middle Stone Age ochre processing and behavioural complexity  
656 in the Horn of Africa: Evidence from Porc-Epic Cave, Dire Dawa, Ethiopia. *PLoS ONE* **11**, e0164793  
657 (2016).
  - 658 53. Hodgskiss, T. Identifying grinding, scoring and rubbing use-wear on experimental ochre pieces. *J.*  
659 *Archaeol. Sci.* **37**, 3344–3358 (2010).
  - 660 54. Rifkin, R. F. Processing ochre in the Middle Stone Age: Testing the inference of prehistoric behaviours  
661 from actualistically derived experimental data. *J. Anthropol. Archaeol.* **31**, 174–195 (2012).
  - 662 55. Rosso, D. E., d’Errico, F. & Queffelec, A. Patterns of change and continuity in ochre use during the late  
663 Middle Stone Age of the Horn of Africa: the Porc-Epic Cave record. *PLoS ONE* **12**, e0177298 (2017).
  - 664 56. Lafuente, B., Downs, R. T., Yang, H. & Stone N. “The power of databases: the RRUFF project” in  
665 Highlights in Mineralogical Crystallography, T. Armbruster, R. M. Danisi, Eds. (W. De Gruyter, 2015) pp.  
666 1–30.
  - 667 57. Bassel, L. et al. Fluorescence-based knife-edge beam diameter measurement to characterize X-ray beam  
668 profiles in reflection geometry. *Spectroc. Acta Pt. B-Atom. Spectr.* **118**, 98–101 (2016).
  - 669 58. Dayet, L. et al. Manganese and iron oxide use at Combe-Grenal (Dordogne, France): A proxy for cultural  
670 change in Neanderthal communities. *J. Archaeol. Sci. Rep.* **25**, 239–256 (2019).
  - 671 59. Queffelec, A., d’Errico, F. & Vanhaeren, M. “Analyse des blocs de matière colorante de Praileaitz I (Deba,  
672 Gipuzkoa)” in Munibe Monographs ([Anthropology and Archaeology Series](#), 2017). pp. 493–503.
  - 673 60. Lucas-Tooth, H. J. and Price, B. J. A mathematical method for the investigation of inter-element effects in  
674 X-ray fluorescence. *Metallurgia* **64**, 149–152 (1961).
  - 675 61. Anthony, J. W., Bideaux, R. A., Bladh, K. W. & Nichols, M. C. *Handbook of Mineralogy* (Mineral Data  
676 Publishing, Tucson Arizona, USA, 1990).
  - 677 62. Hanesch, M. Raman spectroscopy of iron oxides and (oxy)hydroxides at low laser power and possible  
678 applications in environmental magnetic studies. *Geophys. J. Int.* **17**, 941–948 (2009).
  - 679 63. Li, J. H. et al. Micro-XRF study of the troodontid dinosaur *Jianianhualong Tengi* reveals new biological  
680 and taphonomical signals. *Atomic Spectroscopy* **42**, 1–11 (2021).
  - 681 64. Deng, C., Zhu, R., Jackson, M. J., Verosub, K. L. & Singer, M. J. Variability of the temperature-dependent  
682 susceptibility of the Holocene eolian deposits in the Chinese loess plateau: a pedogenesis indicator. *Phys.*  
683 *Chem. Earth (A)* **26**, 873–878 (2001).
  - 684 65. Dunlop, D. J. & Özdemir Ö. *Rock Magnetism: Fundamentals and Frontiers* (Cambridge Univ. Press,  
685 Cambridge, UK, 1997).
  - 686 66. Kruiver, P. P., Dekkers, M. J. & Heslop, D. Quantification of magnetic coercivity components by the  
687 analysis of acquisition curves of isothermal remanent magnetization. *Earth Planet. Sci. Lett.* **189**, 269–276  
688 (2001).
  - 689 67. Jiang, Z. et al. Ferro and antiferromagnetism of ultrafine-grained hematite. *Geochem. Geophys. Geosyst.*  
690 **15**, 2699–2712 (2014).
  - 691 68. Özdemir, Ö. & Dunlop, D. J. Hysteresis and coercivity of hematite. *J. Geophys. Res. Solid Earth* **119**,  
692 2582–2594 (2014).
  - 693 69. Roberts, A. P., Cui, Y. & Verosub, K. L. Wasp-waisted hysteresis loops: mineral magnetic characteristics  
694 and discrimination of components in mixed magnetic systems. *J. Geophys. Res.* **100**, 17909–17924 (1995).
  - 695 70. Yuan, J. et al. Rapid drift of the Tethyan Himalaya terrane before two-stage India-Asia collision. *Natl. Sci.*  
696 *Rev.* **8**, nwaal73, doi:10.1093/nsr/nwaa173 (2021).
  - 697 71. Roberts, A. P. et al. Hematite ( $\alpha$ -Fe<sub>2</sub>O<sub>3</sub>) quantification in sedimentary magnetism: limitations of existing  
698 proxies and ways forward. *Geosci. Lett.* **7**, 8, doi:10.1186/s40562-020-00157-5 (2020).
  - 699 72. Semenov, S. A. *Prehistoric Technology. An Experimental Study of the Oldest Tools and Artefacts From*  
700 *Traces of Manufacture and Wear* (Cory, Adams and Mackay Ltd., London, 1964).
  - 701 73. Hayden, B. (Ed), *Lithic Use-Wear Analysis* (Academic Press, New York, 1979).
  - 702 74. Keeley, L. H. *Experimental Determination of Stone Tools Uses: A Microwear Analysis* (The University of  
703 Chicago Press, Chicago, 1980).
  - 704 75. Vaughan, P. C. *Use-Wear Analysis of Flaked Stone Tools* (The University of Arizona Press, Tucson, 1985).

- 705 76. Knutsson, K. Patterns of tools use. Scanning electron microscopy of experimental quartz tools (Societas  
706 Archaeologica Upsalensis, Uppsala, 1988), vol. 10.
- 707 77. González, J. E. & Ibáñez, J. J. *Metodología de Análisis funcional de instrumentos tallados en sílex*  
708 (Universidad de Deusto, Bilbao, 1994)
- 709 78. Levi Sala, I. *A Study of Microscopic Polish on Flint Implements* (Tempus Reparatum, Oxford, 1996). BAR  
710 IS629.
- 711 79. Marreiros, J. M., Gibaja Bao, J. F. & Ferreira Bicho, N. *Use-Wear and Residue Analysis in Archaeology*  
712 (Springer Cham Heidelberg New York, 2015).
- 713 80. Stemp W. J., Watson A. S. & Evans A. A. Surface analysis of stone and bone tools. *Surf. Topogr. Metrol.*  
714 *Prop.* **4**, 13001 (2016).
- 715 81. Ollé, A. & Vergès, J. M. “SEM functional analysis and the mechanism of microwear formation” in  
716 ‘Prehistoric Technology’ 40 years later: Functional Studies and the Russian Legacy. Proceedings of the  
717 International Congress Verona (Italy), 20-23 April 2005, Longo L., Skakun N., Eds. (Archaeopress,  
718 Oxford, 2008), BAR 1783, pp. 39–49.
- 719 82. Ollé, A. & Vergès, J. M. The use of sequential experiments and SEM in documenting stone tool microwear.  
720 *J. Archaeol. Sci.* **48**, 60–72 (2014).
- 721 83. Fernández-Marchena, J. L. & Ollé, A. Microscopic analysis of technical and functional traces as a method  
722 for the use-wear analysis of rock crystal tools. *Quat. Int.* **424**, 171–190 (2016).
- 723 84. Pedergrana, A. & Ollé, A. Monitoring and interpreting the use-wear formation processes on quartzite  
724 flakes through sequential experiments. *Quat. Int.* **427**, 35–65 (2017).
- 725 85. Borel, A., Ollé, A., Vergès, J. M. & Sala, R. Scanning Electron and Optical Light Microscopy: two  
726 complementary approaches for the understanding and interpretation of usewear and residues on stone tools.  
727 *J. Archaeol. Sci.* **48**, 46–59 (2014).
- 728 86. Ollé, A. et al. Microwear features on vein quartz, rock crystal and quartzite: a study combining Optical  
729 Light and Scanning Electron Microscopy. *Quat. Int.* **424**, 154–170 (2016).
- 730 87. Pedergrana, A., Ollé, A. & Evans, A. A. A new combined approach using confocal and scanning electron  
731 microscopy to image surface modifications on quartzite. *J. Archaeol. Sci. Rep.* **30**, 102237 (2020).
- 732 88. Martín-Viveros, J. I. & Ollé, A. Use-wear and residue mapping on experimental chert tools. A multi-scalar  
733 approach combining digital 3D, optical, and scanning electron microscopy. *J. Archaeol. Sci. Rep.* **30**,  
734 102236 (2020).
- 735 89. Monnier, F., Ladwig, J. & Porter, L. S. T. Swept under the rug: the problem of unacknowledged ambiguity  
736 in lithic residue identification. *J. Archaeol. Sci.* **39**, 3284–3300 (2012).
- 737 90. Pedergrana, A., Asryan, L., Fernández-Marchena, J. L. & Ollé, A. Modern contaminants affecting  
738 microscopic residue analysis on stone tools: A word of caution. *Micron* **86**, 1–21 (2016).
- 739 91. Pedergrana, A. & Ollé, A. Building an experimental comparative reference collection for lithic micro-  
740 residue analysis based on a multi-analytical approach. *J. Archaeol. Method Theory* **25**, 117–154 (2018).
- 741 92. Xhaufclair, H. et al. Use-related or contamination? Residue and use-wear mapping on stone tools used for  
742 experimental processing of plants from Southeast Asia. *Quat. Int.* **427**, 80–93 (2017).
- 743 93. Martín-Viveros, J. I. & Ollé, A. Using 3D digital microscopy and SEM-EDX for in-situ residue analysis: A  
744 multi-analytical contextual approach on experimental stone tools. *Quat. Int.* **569–570**, 228–262 (2020).
- 745 94. Hayes, E., Cnuts, D. & Rots, V. Integrating SEM-EDS in a sequential residue analysis protocol: Benefits  
746 and challenges. *J. Archaeol. Sci. Rep.* **23**, 116–126 (2019).
- 747 95. Ollé, A. Variabilitat i patrons funcionals en els sistemes tècnics de Mode 2. Anàlisi de les deformacions  
748 d’ús en els conjunts lítics del Riparo Esterno de Grotta Paglicci (Rignano Garganico, Foggia), Áridos  
749 (Arganda, Madrid) i Galería-TN (Sierra de Atapuerca, Burgos). Thesis, Universitat Rovira i Virgili,  
750 Tarragona (2003).
- 751 96. Fernández-Marchena, J. L. et al. Rainbow in the dark. The identification of diagnostic projectile impact  
752 features on rock crystal. *J. Archaeol. Sci. Rep.* **31**, 102315 (2020).
- 753 97. Martín-Viveros, J. I. et al. Use-wear analysis of a specific mobile toolkit from the Middle Palaeolithic site  
754 of Abric Romaní (Barcelona, Spain): a case study from level M. *Archaeol. Anthropol. Sci.* **12**, 16 (2020).
- 755 98. Downs, R.T. **The RRUFF Project: an integrated study of the chemistry, crystallography, Raman and**  
756 **infrared spectroscopy of minerals.** Program and Abstracts of the 19th General Meeting of the International  
757 Mineralogical Association in Kobe, Japan. p. 3–13. (2006).

- 758 99. Robertson, D. J. & France, D. E. Discrimination of remanence-carrying minerals in mixtures, using  
759 isothermal remanent magnetisation acquisition curves. *Phys. Earth Planet. Inter.* **82**, 223–234 (1994).  
760 100. Swanson-Hysell, N. L., Fairchild, L. M. & Slotznick, S. P. Primary and secondary red bed  
761 magnetization constrained by fluvial intraclasts. *J. Geophys. Res. Solid Earth* **124**, 4276–4289 (2019).  
762